NJC

PAPER

View Article Online
View Journal | View Issue

Cite this: *New J. Chem.*, 2019, **43**, 18193

Synthesis and comparison of copper(II) complexes with various *N*-aminotetrazole ligands involving trinitrophenol anions†‡

Maximilian H. H. Wurzenberger, Benjamin R. G. Bissinger, Marcus Lommel, Michael S. Gruhne, Norbert Szimhardt and Jörg Stierstorfer *

Due to the ongoing research on lead-free energetic materials, two different ligand systems (1-amino-5*H*-tetrazole (1-AT), 2-amino-5*H*-tetrazole (2-AT), 1-amino-5-methyltetrazole (1-AMT), and 2-amino-5-methyltetrazole (2-AMT)) were applied for the synthesis of 12 new energetic coordination compounds (ECC) with copper(II) as the central metal. Different anions based on trinitrophenols (picric acid (HPA), styphnic acid (H_2TNR), and trinitrophloroglucinol (H_3TNPG)) were used for the specifical tuning of the energetic and physico-chemical properties of the complexes. Through the choice of ligand, the characteristics of the resulting products can be easily adjusted either towards sensitive primary explosives usable for classical initiation setups or towards laser-ignitable explosives with decreased sensitivities. The ECC were extensively characterized by *e.g.*, X-ray diffraction (XRD), elemental analysis (EA), IR, differential thermal analysis (DTA), and UV/vis. In addition, the most promising compounds were analyzed by TGA and in classical initiation tests using nitropenta (PETN). Furthermore, the sensitivities towards external stimuli (impact, friction, and electrostatic discharge) were determined by standard methods and the influence of the anions towards them was investigated. Compounds [Cu(TNR)(1-AMT)$_2$] and [Cu(HTNPG)(1-AMT)$_2$] both possess appropriate sensitivities as well as thermal stabilities above 200 °C and show promising results to be used as potential lead azide replacements. In addition, all ECC were irradiated with a near infrared light (NIR) laser diode leading to different responses.

Received 30th July 2019,
Accepted 28th October 2019

DOI: 10.1039/c9nj03937f

rsc.li/njc

Introduction

The energetic character of many nitroaromatic compounds derives from the oxidation of the carbon-backbone and the circumstance that these substances combine both the fuel (C–H backbone) and the oxidizer (nitro groups) within one molecule. As a result of this, selected polynitroaromatics can be used as explosives, most notably trinitrotoluene (TNT).[1] A close structural relative of TNT is picric acid (HPA, **1**) (Chart 1), which was discovered in the form of its potassium salt by Johann Glauber in 1742.[2]

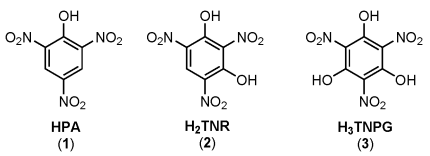

Chart 1 Trinitrophenols picric acid (**1**), styphnic acid (**2**) and trinitrophloroglucinol (**3**).

The compound was obtained *via* treatment of wool or horn with HNO_3 and has since been applied as a dye for silk, and, due to its intensely bitter taste and tinctorial power, as a replacement for hops in beer. However, it wasn't until more than 100 years later that German chemist Hermann Sprengel demonstrated that picric acid could be brought to detonation, and therefore filed the related patents. Following this, HPA replaced black powder in nearly all military applications.[2–4]

Styphnic acid (H_2TNR, **2**) and 2,4,6-trinitrophloroglucinol (H_3TNPG, **3**) derive structurally from picric acid and have a wide history of military applications together with their metal salts. The most prominent is lead styphnate (LS), a rather sensitive and highly toxic primary explosive. Together with lead

Department of Chemistry, Ludwig Maximilian University of Munich, Butenandtstr. 5-13, D-81377 Munich, Germany. E-mail: jstch@cup.uni-muenchen.de; Web: http://www.cup.lmu.de/ac/stierstorfer/, http://www.hedm.cup.uni-muenchen.de; Fax: +49-89-2180-77492

† Parts of this work were presented at the 22nd Seminar on New Trends in Research of Energetic Materials 2019 at the University of Pardubice (Czech Republic).

‡ Electronic supplementary information (ESI) available: Compound overview; IR spectroscopy; X-ray diffraction; TGA plots of **6**, **8**, **11–13**, and **16**; DTA plots of **4b**, **5b**, and **6–17**; column diagrams of the complexes; hot plate and hot needle tests; laser ignition tests; UV-vis spectra of **6–14a** and **15–17**; experimental part and general methods. CCDC 1934798–1934813. For ESI and crystallographic data in CIF or other electronic format see DOI: 10.1039/c9nj03937f

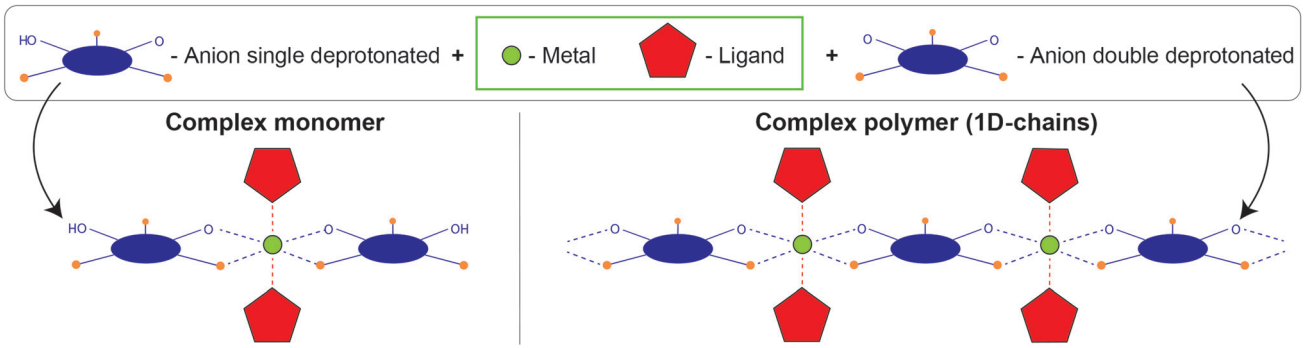

Fig. 1 Schematic overview of the formation of either complex monomers (left) or polymeric structures (right) caused by the deprotonation level of the nitroaromatic anions.

azide (LA), LS has been employed since the beginning of the 20th century and was originally developed as a replacement for mercury fulminate.[2,5] One major drawback of the highly acidic compounds **1–3** is their potential to corrode metal shells, along with the formation of the corresponding highly sensitive metal salts. This process significantly lowers the manageability of such explosives and is known to have caused fatal accidents.[6]

With LA and LS still being the most predominantly used primary explosives *e.g.*, in small arms ammunition, people in frequent contact with firearms and commercial applications (mining, deconstruction works, *etc.*) are at high risk of chronic damage due to heavy metal poisoning. A recent study revealed elevated blood lead levels in regular visitors of shooting ranges, accredited to the discharge of lead upon firing a gun. The adverse health effects associated with shooting are especially critical to women and children, relating to the impact on future generations.[7] In order to reduce or even prevent the use of toxic explosives, scientists all around the world are focusing on the development of new substances with superior properties.[8–15] One very promising concept for replacing toxic primary explosives which has gained increasing attention in recent years is focused on the laser ignition of energetic materials. By combining the right building blocks, this approach could ensure lifelong economic efficiency with environmentally friendly disposal management. At the same time, it can increase safety by allowing the application of less sensitive explosives.[16] 3D Metal coordination compounds with trinitrophenolates of **1–3** as counteranions are known in the literature for only a few tetrazole derivatives, especially TNPG-based anions are rather uncommon. Copper(II) complexes have a unique position among these described compounds since in every single example the anions coordinate to the central metal and thus in almost all cases anhydrous compounds are obtained. Especially, the nitroaromatic complexes based on Mn(II), Co(II), Ni(II) and Zn(II) have a high tendency to incorporate aqua ligands, crystal water molecules or even both of them.[17–23] Another characteristic of styphnic acid and trinitrophloroglucinol is their ability to work either as singly or multiply deprotonated anions and it has also been shown that within one ligand system both cases can be obtained. A great advantage of the twofold deprotonation of trinitrophenols is their potential to bridge different metal centres. In contrast, abstraction of a single proton usually leads to complex monomers (Fig. 1).[24]

The linking of the anions allows the formation of polymeric structures with varying properties such as increased thermal stabilities.

Recently, our research group published several of the most powerful ECC available, based on 1-amino-5*H*-tetrazole (1-AT) and 2-amino-5*H*-tetrazole (2-AT), in combination with highly oxidizing anions such as perchlorate and nitrate.[25] Some of the most auspicious of these candidates combine excellent energetic properties with good thermal stabilities and low environmental toxicities, however, the highly endothermic aminotetrazole ligands and oxidizing anions induce extreme sensitivities to various mechanical stimuli. This diminishes their applicability as primary explosives in classical, as well as optical initiation systems. To manage the excessive energetic capacities and sensitivities of 1-AT and 2-AT based ECC, we replaced the common anions nitrate and perchlorate with nitroaromatic mono- and dianions of **1–3**. Furthermore, an additional methyl group was introduced at the 5-position of the ligands (1-amino-5-methyltetrazole (1-AMT) and 2-amino-5-methyltetrazole (2-AMT)) to further stabilize the system by lowering the enthalpies of formation (Fig. 2).

This extensive study describes the effect of various *N*-amino-tetrazole ligands on nitroaromatic copper(II) complexes and

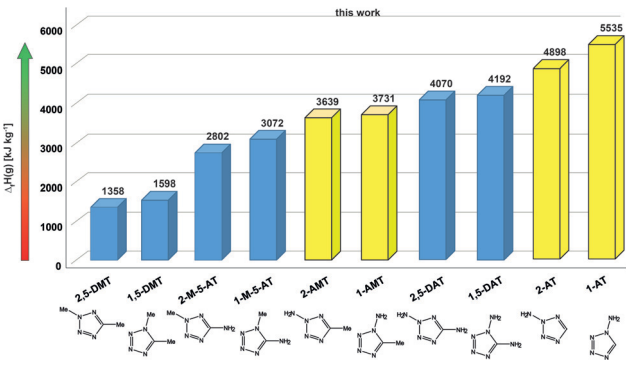

Fig. 2 Comparison of the calculated enthalpies of formation for several *N*-substituted monotetrazoles showing decreased values for AMT ligands compared to AT. Gas phase enthalpies of formation were calculated using the atomization method ($\Delta_f H^0_{(g,M)} = H_{(M)} - \sum H^0_{(A)} + \sum \Delta_f H^0_{(A)}$) using Gaussian09 computed CBS-4M electronic enthalpies.

their selective potential to be used as either laser ignitable explosives or as classical lead-free primary explosives for the initiation of PETN (nitropenta). Furthermore, the influence of the level of deprotonation as well as the number of hydroxy groups in the anions towards the properties of the ECC is compared.

Results and discussion

Synthesis

1-AMT (**4b**) and 2-AMT (**5b**) were prepared in accordance with the synthesis[25] of **4a** and **5a** *via* nucleophilic amination of commercially available 5-methyl-1*H*-tetrazole with hydroxylamine-*O*-sulfonic acid under basic conditions, giving the isomers **4b** and **5b** in 33% and 25% yield, respectively (Scheme 1). Due to the positive inductive effect of the additional methyl group, which increases the nucleophilicity of the electron-poor heterocycle, the overall yield of the reaction could be increased compared to the amination of unsubstituted tetrazole (58% *vs.* 46%).

In analogy to **4a**, 1-AMT can be obtained directly and isomerically pure *via* a simple and scalable three-step reaction.[25] The synthesis is initiated by the condensation of benzaldehyde and hydrazine hydrate, followed by [3+1+1] cyclization with sodium azide and triethyl orthoacetate, which generates the 5-methyltetrazole-moiety (**4b_pro**). Cleavage under acidic conditions followed by water steam distillation furnishes the ligand **4b** in a relatively low yield of 18% (Scheme 2).

The isomers **4b** and **5b** can easily be differentiated by IR (Fig. S1, ESI‡) or by ^{1}H and ^{13}C NMR spectroscopy. Furthermore, proton coupled ^{15}N NMR measurements were performed for both compounds (Fig. 3 and 4).

The synthesis of ECC **6–17** starts with the *in situ* generation of the copper(II) salt of the required trinitrophenol, which is

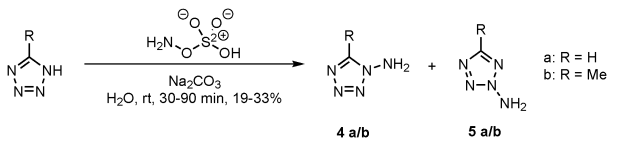

Scheme 1 Synthesis of aminotetrazole ligands **4** and **5** by amination of 1*H*-tetrazole with hydroxylamine-*O*-sulfonic acid (HOSA).

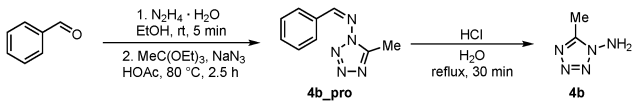

Scheme 2 Selective synthesis of 1-amino-5-methyltetrazole (1-AMT, **4b**).

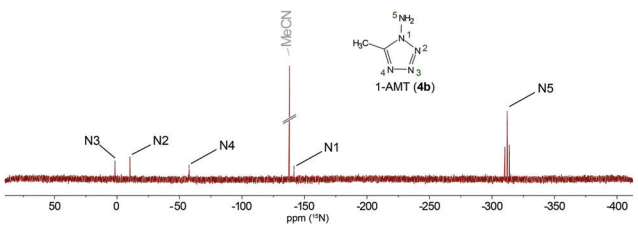

Fig. 3 Proton coupled ^{15}N NMR spectra of **4b**.

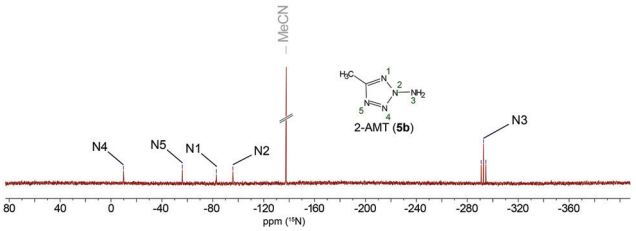

Fig. 4 Proton coupled ^{15}N NMR spectra of **5b**.

achieved by reaction of copper(II) carbonate with the respective acid **1–3** in aqueous medium at elevated temperatures. In the case of amino-5*H*-tetrazole derivates, each of the performed syntheses was carried out by slow addition of an aqueous solution of the ligand to the respective solution of metal(II) salt at 80 °C (Schemes 3 and 4). After continuous stirring of the particular reaction mixture, the solutions were left for crystallization at room temperature. After a few days, the compounds were filtered off, washed with ethanol and dried in air. This synthetic strategy can easily be performed on a large scale and the products can be isolated almost quantitatively if the solvent of the reaction mixture is removed by rotary evaporation.

Synthesis of the analogous AMT-based complexes **12–17** proceeded identically (Schemes 5 and 6), the only noteworthy divergence being the immediate precipitation of green and brown solids during the synthesis of compounds **13** and **14a**, respectively. Both compounds form polymeric structures that arise from the twofold deprotonation of the corresponding anions (**13**: styphnate, **14a**: 5-hydroxy-2,4,6-trinitroresorcinate) leading to bridging between different central metals, which significantly reduces their water solubility. All other isolated AMT-complexes were obtained after crystallisation from the mother liquor within a few days. After formation, the products were filtered off, washed with ethanol and dried in air. Even though final products **13** and **14a** are formed of only one

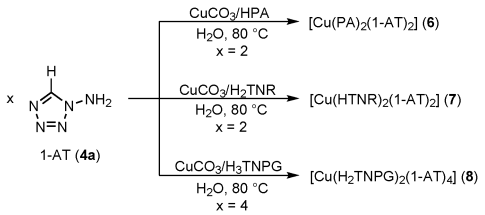

Scheme 3 Synthesis of copper(II) picrate, 3-hydroxy-2,4,6-trinitrophenolate and 3,5-dihydroxy-2,4,6-trinitrophenolate complexes **6–8** of 1-AT (**4a**).

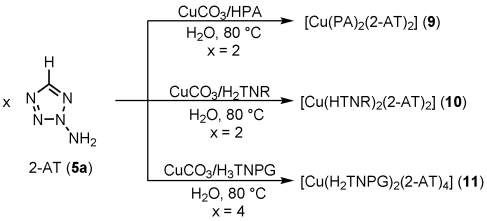

Scheme 4 Synthesis of the ECC **9–11** based on 2-amino-5*H*-tetrazole (2-AT, **5a**).

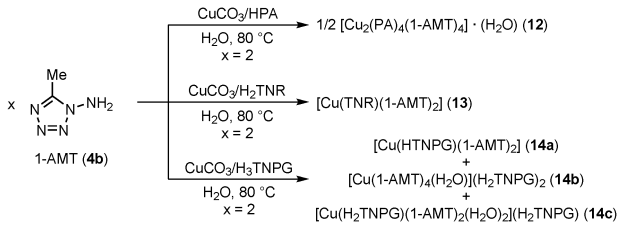

Scheme 5 Synthesis of copper(II) picrate (PA), styphnate (TNR) and 2,4,6-trinitrophloroglucol-based (HTNPG/H_2TNPG) complexes of 1-amino-5-methyltetrazole (1-AMT, **4b**).

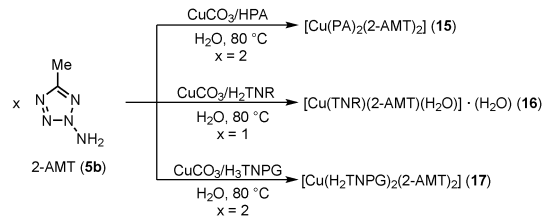

Scheme 6 Synthesis of ECC **15–17** based on 2-amino-5-methyltetrazole (2-AMT, **5b**).

equivalent of the corresponding anions, for complete reaction of copper(II) carbonate twice the amount of free acid is required. Interestingly, the formation of a second (**14b**) and a third (**14c**) species during the reaction of copper(II) carbonate, trinitrophloroglucinol and 1-AMT was observed.

Single crystal experiments reveal the composition of two different aqua complexes $[Cu(1\text{-}AMT)_4(H_2O)](H_2TNPG)_2$ (**14b**) and $[Cu(H_2TNPG)(1\text{-}AMT)_2(H_2O)_2](H_2TNPG)$ (**14c**) with only singly deprotonated anions (3,5-dihydroxy-2,4,6-trinitrophenolate). The dark green needles of **14a** crystallised quickly from the filtrate and accumulated on the inner walls of the crystallisation vessel. Contrary to **14a**, however, **14b** turned out to be extremely water-soluble, which prevented the execution of further analytical investigation, because sufficient amounts could not be isolated. Similar to **14b**, **14c** is highly water soluble and some single crystals could only be obtained after complete desiccation of the filtrate of **14a**. To the best of our knowledge, **14b** and **14c** are the first copper(II) complexes with non-coordinating counteranions based on trinitrophenols of **1–3**.

Compared to the anhydrous compounds **6–11** it becomes clear that the AMT ligands slightly increase the hydrophilicity of the formed products and thus the formation of complexes with aqua ligands (**14b** and **14c**), crystal water molecules (**12**) or even both of them (**16**) can partly be observed.

Crystal structures

Nitrogen-rich ligand **4b** and its precursor **4b_pro**, as well as all ECC, were investigated by low-temperature single crystal X-ray diffraction. In contrast to their 1-amino isomers, 2-AT (**5a**) and 2-AMT (**5b**) were not able to be crystallised, even when subjected to liquid nitrogen. The crystal structure of ligand **4a** has already been published;[25] the results of the crystallographic analysis of **4b_pro** (Fig. S4, ESI‡) are given in the ESI,‡ together with the measurement and refinement data of all experiments (Tables S1–S4, ESI‡). The crystal datasets were uploaded to the CSD database[26] and can be obtained free of charge with the CCDC 1934808 (**4_pro**), 1934810 (**4b**), 1934799 (**6**), 1934801 (**7**), 1934798 (**8**), 1934809 (**9**), 1934811 (**10**), 1934812 (**11**), 1934806 (**12**), 1934805 (**13**), 1934803 (**14a**), 1934807 (**14b**), 1934813 (**14c**), 1934800 (**15**), 1934802 (**16**), and 1934804 (**17**). All complexes, except side species **14b**, show octahedral coordination spheres around the copper(II) central cations with typical Jahn–Teller distortions along the axial O–Cu–O axes. In every structure, the ligands are solely coordinated through the N4 nitrogen atom of the tetrazole rings. In almost all compounds electrostatic intermolecular interactions can be observed, leading to specific orientations of the nitro groups of the phenolate anions. Normally the nitro groups of the trinitrophenols are aligned with the aromatic system, while nitro–nitro interactions between different anions twist one or two of the functional groups in the complexes. This perpendicular arrangement of nitro groups enables the electrostatic interaction of the vertical π-orbital with the oxygen atom of a second nitro group. The distances O_{Nitro}–π$(N)_{Nitro}$ in the crystal structures lie in the typical range of nitro–nitro interactions described in the literature.[27]

Similar to **4a**,[25] tetrazole **4b** crystallises in the orthorhombic space group $P2_12_12_1$ with four formula units per unit cell and a slightly lower calculated density of 1.420 g cm^{-3} at 143 K. This relatively significant difference in density arises from the presence of the methyl group in **4b**, preventing closer packing due to the increased steric hindrance (Fig. 5). It crystallises in the form of colourless blocks and all non-hydrogen atoms lie within a plane with torsion angles close to 0° (C1–N1–N2–N3 1.25(15)°, N5–N1–C1–C2 −2.2(2)°, and N2–N1–C1–N4 −1.13(16)°). The bond angles and lengths lie within the range of typical values for tetrazole compounds and differ only slightly from 1-AT.

Picrate compounds **6** (green platelets) and **12** (green blocks) crystallise in similar monoclinic space groups $P2_1/c$ and $P2_1/n$ with calculated densities of 1.952 g cm^{-3} and 1.786 g cm^{-3} at 143 K, respectively. The slightly distorted octahedral coordination spheres – **12** shows a stronger deviation than **6** – around the

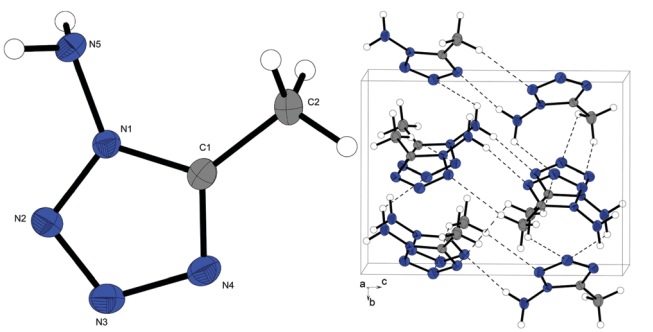

Fig. 5 Molecular unit (left) and unit cell (right) of 1-AMT (**4b**). Thermal ellipsoids of nonhydrogen atoms in all structures are set to the 50% probability level. Selected bond lengths (Å): N1–N2 1.3482(16), N1–N5 1.3908(17), N1–C1 1.3341(18), N2–N3 1.2959(19), N3–N4 1.3648(19), N4–C1 1.3206(19); selected bond angles (°): N2–N1–N5 123.54(11), N2–N1–C1 109.92(12), N5–N1–C1 126.53(12), N3–N4–C1 106.14(12), N4–C1–C2 127.78(13).

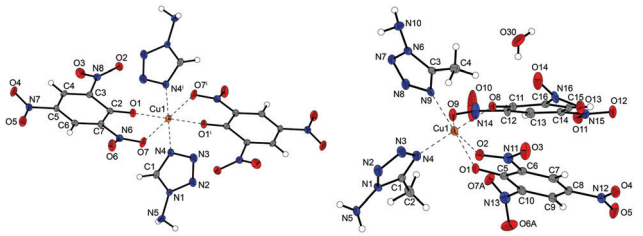

Fig. 6 Molecular unit of $[Cu(PA)_2(1\text{-}AT)_2]$ (**6**) (left) and segment of the unit cell of $[Cu_2(PA)_4(1\text{-}AMT)_4]\cdot H_2O$ (**12**) (right). Selected bond lengths (Å) of **6**: Cu1–O1 1.918(3), Cu1–O7 2.338(3), Cu1–N4 2.010(3); selected bond angles (°) of **6**: O1–Cu1–O7 78.92(10), O1–Cu1–N4 90.18(12), O7–Cu1–N4 86.01(11). Symmetry code of **6**: (i) $2 - x, -y, 2 - z$. Selected bond lengths (Å) of **12**: Cu1–O2 2.467(3), Cu1–O8 1.946(3), Cu1–N4 1.972(3), Cu1–N9 1.995(3); selected bond angles (°) of **12**: O1–Cu1–O2 74.07(11), O1–Cu1–N4 90.31(13), O1–Cu1–N9 171.19(13), N4–Cu1–N9 89.82(14).

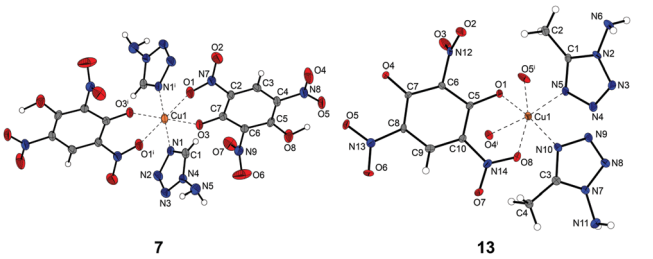

Fig. 7 Molecular unit of $[Cu(HTNR)_2(1\text{-}AT)_2]$ (**7**) (left) and the copper(II) coordination environment of $[Cu(TNR)(1\text{-}AMT)_2]$ (**13**) (right). Selected bond lengths (Å) of **7**: Cu1–O1 2.316(3), Cu1–O3 1.962(2), Cu1–N1 1.998(3); selected bond angles (°) of **7**: O1–Cu1–O3 81.17(10), O1–Cu1–N1 87.63(12), O3–Cu1–N1 90.00(11). Symmetry code of **7**: (i) $2 - x, 1 - y, 1 - z$. Selected bond lengths (Å) of **13**: Cu1–O1 1.958(5), Cu1–O8 2.515(6), Cu1–N5 1.994(6), Cu1–N10 2.010(6); selected bond angles (°) of **13**: O1–Cu1–O8 72.54(16), O1–Cu1–N5 86.0(2), O1–Cu1–N10 167.1(2), N5–Cu1–N10 94.7(2). Symmetry code of **13**: (i) $1 - x, 2 - y, 0.5 + z$.

copper(II) central cations in both crystal structures show similar compositions. The central metals are surrounded by two monodentate tetrazole ligands and two chelating picrate anions. $[Cu(PA)_2(1\text{-}AT)_2]$ (**6**) represents a centrosymmetric unit in itself with *trans* coordinating 1-AT ligands, while in $[Cu_2(PA)_4(1\text{-}AMT)_4]\cdot H_2O$ (**12**) the pairs of ligand molecules and picrate anions each occupy adjacent coordination sites (Fig. 6). The molecular unit of picrate **12** is a dimer consisting of two of the previously described asymmetric units and an additional crystal water molecule, where the coordinating picrate anions are facing each other in the centre of the unit and are twisted against each other at angles of approximately 90°.

Complexes **7** and **13**, based on 2,4,6-trinitroresorcinol, crystallise in the monoclinic and orthorhombic space groups $P2_1/c$ and $Pna2_1$ as green platelets and needles, respectively. Their calculated densities of 1.905 g cm^{-3} and 1.887 g cm^{-3} at 143 K vary only slightly. Except for the crystal water molecule, the compounds' chemical building blocks and the arrangement of those are comparable to those of the analogue picrate complexes **6** and **12**. ECC **7** forms complex monomers with a highly symmetrical structure, in which 1-AT and anionic 3-hydroxy-2,4,6-trinitrophenolate ligands oppose each other.

In fact, both coordinating molecules of 1-AT lie in the same plane and are aligned perfectly parallel, the singly deprotonated anions span two parallel planes. In 1-AMT-based compound **13** the pairs of ligand molecules and styphnate anions again occupy adjacent coordination sites (Fig. 7). The twofold deprotonation of styphnic acid in **13** leads to the formation of 1D-polymeric chains, in which each dianion bridges between two copper(II) centres. The monoanions existent in **7** are not suitable for linking between metal centres as they only possess a single coordination site, and thus two of them are required per formula unit.

Comparing the styphnate complexes **7** and **13** with the analogous trinitrophloroglucinol-based compounds, it becomes clear that the complexation of the central metal is different in the case of **8** and almost identical for **14a**. They crystallise in the monoclinic space group $P2_1/n$ (**8**) as green-yellow rods and orthorhombic space group $Pna2_1$ (**14a**) as brown needles with calculated densities of 1.928 g cm^{-3} (173 K) and 1.891 g cm^{-3} (143 K), respectively. The crystal structure of **8** is composed of four neutral 1-AT ligands and two 3,5-dihydroxy-2,4,6-trinitrophenolate monoanions around octahedrally coordinated copper(II) centres. The singly deprotonated anions are monodentate and are building up the Jahn–Teller distorted along the axial O1–Cu–O1^{i} axis (Fig. 8). All equatorial positions are occupied by tetrazole derivatives, which form hydrogen bonds with their amino function to nitro groups of the anions and tetrazole rings of neighbouring complex monomers. The primary species obtained from copper(II) carbonate, trinitrophloroglucinol and 1-AMT, $[Cu(HTNPG)(1\text{-}AMT)_2]$ (**14a**), crystallises isotypically to **13** with similar cell axes, density, and cell volume. Again, the double deprotonation leads to higher distortion and the formation of polymeric 1D chains. The coordination polymer is otherwise almost identical to **13**.

The side species **14b** and **14c** both crystallise as green rods in monoclinic space groups ($P2_1/c$ and $P2_1/n$) with calculated densities of 1.798 g cm^{-3} (143 K) and 1.948 g cm^{-3} (111 K), respectively. While **14b** shows a rare square pyramidal coordination sphere around the copper(II) centre, the coordination sphere of **14c** is a

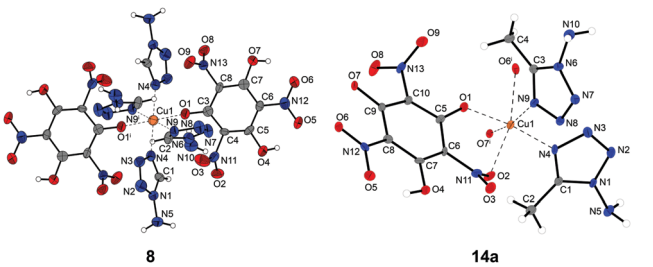

Fig. 8 Molecular unit of $[Cu(H_2TNPG)_2(1\text{-}AT)_4]$ (**8**) (left) and the copper(II) coordination environment of $[Cu(HTNPG)(1\text{-}AMT)_2]$ (**14a**) (right). Selected bond lengths (Å) of **8**: Cu1–O1 2.348(4), Cu1–N4 2.015(5), Cu1–N9 1.986(5); selected bond angles (°) of **8**: O1–Cu1–N4 87.64(17), O1–Cu1–N9 96.28(17), N4–Cu1–N9 91.1(2). Symmetry code of **8**: (i) $1 - x, 1 - y, 1 - z$. Selected bond lengths (Å) of **14a**: Cu1–O1 1.933(4), Cu1–O2 2.252(5), Cu1–N4 1.985(6), Cu1–N9 2.007(6); selected bond angles (°) of **14a**: O1–Cu1–O2 81.56(18), O1–Cu1–N4 171.7(2), O1–Cu1–N9 90.8(2), N4–Cu1–N9 95.5(2). Symmetry code of **14a**: (i) $1 - x, 1 - y, -0.5 + z$.

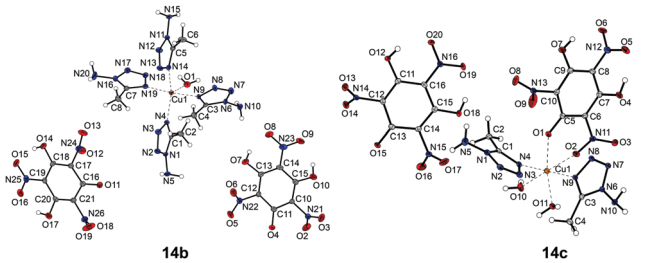

Fig. 9 Molecular units of side species $[Cu(1\text{-}AMT)_4(H_2O)](H_2TNPG)_2$ (**14b**) (left) and $[Cu(H_2TNPG)(1\text{-}AMT)_2(H_2O)_2](H_2TNPG)$ (**14c**) (right). Selected bond lengths (Å) of **14b**: Cu1–O1 2.230(3), Cu1–N4 2.000(3), Cu1–N9 2.005(3), Cu1–N14 1.997(3), Cu1–N19 1.997(3); selected bond angles (°) of **14b**: O1–Cu1–N4 103.93(12), O1–Cu1–N9 87.27(12), N4–Cu1–N9 92.78(12), N4–Cu1–N14 149.23(11), N4–Cu1–N19 92.08(12), N9–Cu1–N19 174.14(12). Selected bond lengths (Å) of **14c**: Cu1–O1 1.9934(15), Cu1–O11 2.0671(17), Cu1–N4 1.9784(16), Cu1–N9 1.9856(16); selected bond angles (°) of **14c**: O1–Cu1–O2 74.84(6), O1–Cu1–O10 107.90(6), O1–Cu1–O11 163.97(6), O1–Cu1–N4 88.60(7), O1–Cu1–N9 91.36(7), N4–Cu1–N9 179.38(7).

highly distorted octahedron. In contrast to **14a**, **14b** possesses non-coordinating anions and, similar to **8**, **11** and **17**, the TNPG-based monoanions are present as 3,5-dihydroxy-2,4,6-trinitrophenolates stacked on top of each other. They form hydrogen bonds to amino groups of neighbouring tetrazole ligands and typical nitro–nitro interactions between each other. The coordination sphere around the copper(II) central metal in **14b** is composed of one aqua and four ligand molecules of 1-AMT (Fig. 9). The water molecule represents the tip of the pyramid with a slightly longer Cu–O bond (2.230 Å) compared to the Cu–N bonds (1.997–2.005 Å). To minimise steric hindrance, pairs of opposing tetrazole ligands are arranged with the methyl groups facing in alternating directions and the two heterocycles are slightly angled, leading to a distorted plane of coordinating nitrogen atoms (N14–N4–N9–N19 23.7(1)°). The molecular unit of **14c** consists of one non-coordinating and one chelating monoanion, as well as two aqua and two tetrazole ligands. Interestingly, the Jahn–Teller distortion along the O2–Cu1–O10 axis shows one very long Cu–O bond (Cu1–O2 2.4665(14)), while the second is only slightly elongated (Cu1–O10 2.1604(16)).

Even though the coordination environments of the copper(II) centres of picrate complexes **9** and **15** are almost identical and show similar densities (**9**: 1.905 g cm^{-3} @ 173 K; **15**: 1.860 g cm^{-3} @ 143 K), they crystallise in fundamentally different space groups. $[Cu(PA)_2(2\text{-}AT)_2]$ (**9**) crystallises as green needles in the monoclinic $P2_1/c$ and $[Cu(PA)_2(2\text{-}AMT)_2]$ (**15**) as green blocks in the triclinic space group $P\bar{1}$. The equatorial positions are occupied by deprotonated hydroxyl groups and two *trans* coordinating aminotetrazole ligands. In the case of 2-AT based complex **9**, the two heterocycles are aligned anti-parallel, whereas, in complex **15**, the 2-AMT molecules are roughly mirrored in the equatorial plane. The axial positions are occupied by two nitro functions of the picrate anion (Fig. 10). Whereas **9**, similar to picrate complex **6**, shows highly symmetric coordination of the ligands, compound **15** possesses a greater deviation from the perfect octahedron. It is the only

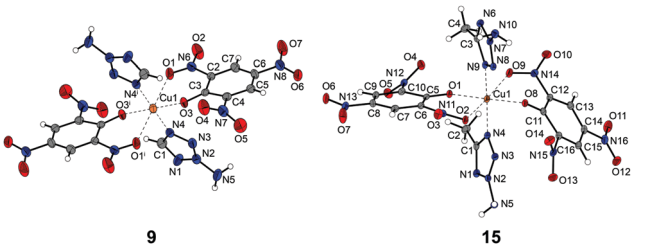

Fig. 10 Molecular unit of $[Cu(PA)_2(2\text{-}AT)_2]$ (**9**) (left) and $[Cu(PA)_2(2\text{-}AMT)_2]$ (**15**) (right). Selected bond lengths (Å) of **9**: Cu1–O1 2.321(2), Cu1–O3 1.941(2), Cu1–N4 1.982(3); selected bond angles (°) of **9**: O1–Cu1–O3 80.03(9), O1–Cu1–N4 87.69(10), O3–Cu1–N4 92.42(10). Symmetry code of **9**: (i) $-x, 1-y, 1-z$. Selected bond lengths (Å) of **15**: Cu1–O1 1.933(2), Cu1–O2 2.335(2), Cu1–N4 2.003(2); selected bond angles (°) of **15**: O1–Cu1–O2 80.73(8), O1–Cu1–N4 89.67(9), O2–Cu1–N4 88.15(9).

AMT-based compound with methyl groups pointing in the same direction, leading to higher steric hindrance (N4–Cu1–N9 172.08(10)°) and thus lower symmetry.

Styphnate compound **10** shows an almost identical composition to its 1-AT isomer **7** and crystallises in the triclinic space group $P\bar{1}$ with a calculated density of 1.864 g cm^{-3} at 173 K in the form of green blocks. Its 5-methyltetrazole analogue **16** crystallises as green rods in the monoclinic space group $P2_1/c$ with a calculated density of 1.949 g cm^{-3} at 143 K. The only similarity with its 1-AMT analogue **13** is the formation of polymer strands due to the twofold deprotonation of the anion. However, complex **16** only contains one neutral heterocycle and an additional aqua ligand, which are located *cis* to each other (Fig. 11). Also, a molecule of crystal water is present in **16**, which is fixed inside the structure by four hydrogen bonds.

3,5-Dihydroxy-2,4,6-trinitrophenolate complexes **11** and **17** both crystallise as green blocks in the triclinic space group $P\bar{1}$ with similar calculated densities of 1.909 g cm^{-3} (173 K) and 1.939 g cm^{-3} (143 K), respectively. Again, **11** shows an identically constructed coordination sphere to 1-AT isomer **8** with four 2-AT ligands in the equatorial plane and monodentate H_2TNPG monoanions in axial positions. Compared to **11**, the octahedron in complex **17** consists only of two tetrazole ligands, and once again

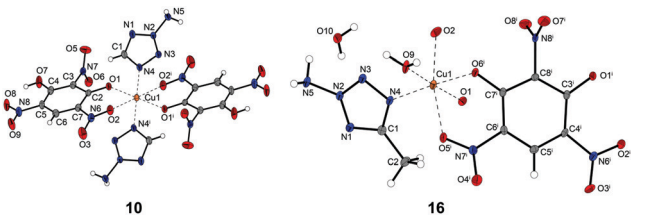

Fig. 11 Molecular unit of $[Cu(HTNR)_2(2\text{-}AT)_2]$ (**10**) (left) and extended molecular unit of $[Cu(TNR)(2\text{-}AMT)(H_2O)]\cdot H_2O$ (**16**) (right). Selected bond lengths (Å) of **10**: Cu1–O1 1.9410(12), Cu1–O2 2.3932(13), Cu1–N4 1.9858(14); selected bond angles (°) of **10**: O1–Cu1–O2 78.44(5), O1–Cu1–N4 88.72(6), O2–Cu1–N4 88.65(5). Symmetry code of **10**: (i) $-x, 2-y, -z$. Selected bond lengths (Å) of **16**: Cu1–O1 1.941(2), Cu1–O2 2.284(2), Cu1–O9 1.968(2), Cu1–N4 2.005(2); selected bond angles (°) of **16**: O1–Cu1–O2 82.20(8), O1–Cu1–O9 176.78(9), O1–Cu1–N4 90.48(8), O2–Cu1–N4 92.83(9), O9–Cu1–N4 92.70(10). Symmetry code of **16**: (i) $1-x, -0.5+y, 0.5-z$.

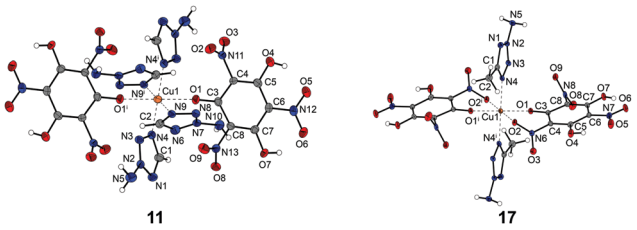

Fig. 12 Molecular unit of $[Cu(H_2TNPG)_2(2\text{-}AT)_4]$ (**11**) (left) and $[Cu(H_2TNPG)_2(2\text{-}AMT)_2]$ (**17**) (right). Selected bond lengths (Å) of **11**: Cu1–O1 2.3614(18), Cu1–N4 2.007(2), Cu1–N9 2.0101(19); selected bond angles (°) of **11**: O1–Cu1–N4 88.38(7), O1–Cu1–N9 95.38(7), N4–Cu1–N9 89.16(9). Symmetry code of **11**: (i) $1 - x$, $1 - y$, $-z$. Selected bond lengths (Å) of **17**: Cu1–O1 1.9180(19), Cu1–O2 2.354(2), Cu1–N4 2.022(3); selected bond angles (°) of **17**: O1–Cu1–O2 81.50(9), O1–Cu1–N4 91.12(10), O2–Cu1–N4 92.03(10). Symmetry code of **17**: (i) $-x$, $1 - y$, $-z$.

two H_2TNPG monoanions, which are in this case chelating (Fig. 12). The presence of the anions as 3,5-dihydroxy-2,4,6-trinitrophenolate (like in **8**, **11**, **14b**, and **14c**) is preventing the bridging between different copper(II) centres.

Sensitivities and thermal stability

Ligands **4b** and **5b**, as well as energetic complexes **6–17**, with the exception of side-products **14b** and **14c**, were subjected to differential thermal analysis (DTA) by heating at a constant rate of β = 5 °C min^{-1} in the temperature range of 25–400 °C. Critical points, such as dehydration, loss of a coordinating ligand or decomposition, are listed in Table 1 and are given as onset temperatures. The DTA plots can be found in the ESI‡ (Fig. S18–S30). All investigated compounds exhibit exothermic decomposition temperatures above 170 °C. Five of the examined ECC (**9**, **10**, **13**, **14a**, and **17**) even surpass a decomposition temperature of 200 °C. Styphnate **13**, the compound with the highest decomposition temperature of all investigated complexes (T_{exo} = 212 °C) derives its high thermal stability from its polymeric structure. A similar case can be observed in ECC **14a** (T_{exo} = 202 °C) with bridging trinitrophenolate anions. However, the relatively low decomposition temperature of the only other 2-AMT-based coordination polymer **16** (T_{exo} = 172 °C) can be explained by the presence of aqua ligands and crystal water molecules. The loss of both (T_{endo} = 122 °C and 160 °C) destabilises the crystal structure, leading to a lower exothermic decomposition temperature. Comparison of the 1-AMT complexes to those featuring 5*H*-tetrazole ligands reveals higher exothermic stabilities for the methyltetrazole based compounds. In the case of the 2-amino isomers, it is the other way round. The ECC based on 2-AT are thermally more stable than the analogous 2-AMT complexes. Apart from **16**, an endothermic peak is only observed in the DTA plot of **11** and is caused by the evaporation of coordinating 2-AT ligands. More detailed investigations using thermal gravimetric analysis (TGA) reveals the loss of two tetrazole derivatives (≙18.4%) starting at 135 °C (Fig. 13).

TGA measurements of ECC **6**, **8**, **11–13** and **16** clearly show the loss of water molecules in **12** and **16** and no significant mass loss in the other measured compounds, which proves their thermal stability up to the corresponding exothermic decomposition points (Fig. S17, ESI‡).

Due to the fact that the crystal morphology has a high effect on sensitivities as well as performance parameters (*e.g.*, a higher sensitivity against ESD with decreasing crystal size[30]), the compounds' grain size and habit were determined by light microscopy (Fig. S5 and S16, ESI‡). The sensitivities towards impact (IS) and friction (FS) of the compounds were determined according to BAM standard techniques (1 of 6) and they

Table 1 Data of thermal stability measurements by DTA,[a] as well as sensitivities towards various external stimuli and results of hot plate (HP) and hot needle (HN) experiments of **4a-5b** and **6–17**

	T_{endo}[b] (°C)	T_{exo}[c] (°C)	IS[d] (J)	FS[e] (N)	ESD[f] (mJ)	BDIS[g] (mJ)	HP[h]	HN[h]
1-AT (**4a**)	—	182[23]	<1[28]	64[28]	n.d.	n.d.	n.d.	n.d.
2-AT (**5a**)	—	197[23]	<1[28]	36[28]	n.d.	n.d.	n.d.	n.d.
1-AMT (**5b**)	—	190	>40	360	n.d.	n.d.	n.d.	n.d.
2-AMT (**5b**)	—	176	35	>360	n.d.	n.d.	n.d.	n.d.
$[Cu(PA)_2(1\text{-}AT)_2]$ (**6**)	—	178	4	120	50	207	def.	def.
$[Cu(HTNR)_2(1\text{-}AT)_2]$ (**7**)	—	186	1.5	48	16	14	def.	def.
$[Cu(H_2TNPG)_2(1\text{-}AT)_4]$ (**8**)	—	193	3.5	20	90	14	def.	def.
$[Cu(PA)_2(2\text{-}AT)_2]$ (**9**)	—	203	3	128	60	>207	def.	def.
$[Cu(HTNR)_2(2\text{-}AT)_2]$ (**10**)	—	206	3	48	20	55	def.	def.
$[Cu(H_2TNPG)_2(2\text{-}AT)_4]$ (**11**)	135	176	2	24	100	14	def.	def.
$[Cu_2(PA)_4(1\text{-}AMT)_4]\cdot H_2O$ (**12**)	—	190	2	168	88	>207	def.	def.
$[Cu(TNR)(1\text{-}AMT)_2]$ (**13**)	—	212	2	16	6.3	10	def.	def.
$[Cu(HTNPG)(1\text{-}AMT)_2]$ (**14a**)	—	202	1	7	4.9	8	def.	det.
$[Cu(PA)_2(2\text{-}AMT)_2]$ (**15**)	—	176	2.5	108	37	>207	def.	def.
$[Cu(TNR)(2\text{-}AMT)(H_2O)]\cdot H_2O$ (**16**)	122, 160	172	2.5	38	840	69	def.	def.
$[Cu(H_2TNPG)_2(2\text{-}AMT)_2]$ (**17**)	—	202	2	20	8.2	41	def.	def.
$Pb(N_3)_2$[29]		320–360	2.5–4.0	0.1–1.0	7.0	n.d.	det.	det.
PETN[29]	141–143	163–170	3.0–4.2	73	60	n.d.	def.	def.

[a] Onset temperatures at a heating rate of 5 °C min^{-1}. [b] Endothermic peak, which indicates melting, dehydration or loss of coordinating molecules. [c] Exothermic peak, which indicates decomposition. [d] Impact sensitivity according to the BAM drophammer (method 1 of 6). [e] Friction sensitivity according to the BAM friction tester (method 1 of 6). [f] Electrostatic discharge sensitivity (OZM Electric XSpark10) (method 1 of 6). [g] Ball drop impact sensitivity determined with method 1 of 6 in accordance with MIL-STD 1751A (method 1016). [h] def.: deflagration, det.: detonation, dec.: decomposition.

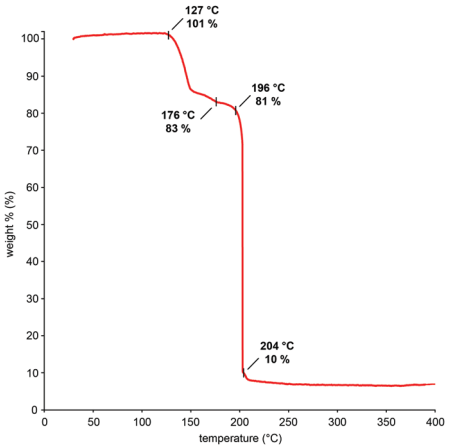

Fig. 13 TGA plot of **11** showing the loss of two aminotetrazole ligands starting at 127 °C followed by the decomposition of the compound.

have been classified in accordance with the "UN Recommendations on the Transport of Dangerous Goods".[31] Furthermore, the electrostatic discharge sensitivity (ESD) of all isolated ECC was analysed and all measurement data are summarised in Table 1. Comparing the free ligands, it becomes clear that the additional methyl group in 1-AMT and 2-AMT is drastically increasing the stability of the aminotetrazole derivatives against external stimuli. Concerning the impact sensitivity, all ECC show similar values against impact and except **6** and **8** ("sensitive") have to be classified as "very sensitive". In the case of FS, a clear trend is observable, revealing an increase of the sensitivity with the number of hydroxy groups of the anion (Fig. 14 and Fig. S31–S33, ESI‡), leading to the general trend: PA (all friction "sensitive") < TNR ("very sensitive") ≤ TNPG ("very sensitive" or even "extremely sensitive" (**14a**)). Due to the more realistic conditions during ball drop impact sensitivity (BDIS) measurements, ECC **6–17** were all tested and show a similar trend in comparison to the determined FS. This confirms our previous findings[22] that the sensitivity against ball drop impact shows a higher correlation with FS than with IS. Interestingly, ECC **13** and **14a**, based on a less sensitive ligand, both show the most sensitive values against external stimuli. The multiple deprotonations of nitroaromatic anions lead not only to higher thermal stability but also to increased sensitivities. This concept can be used for the synthesis and design of sensitive but thermally stable primary explosives for classical initiation devices.

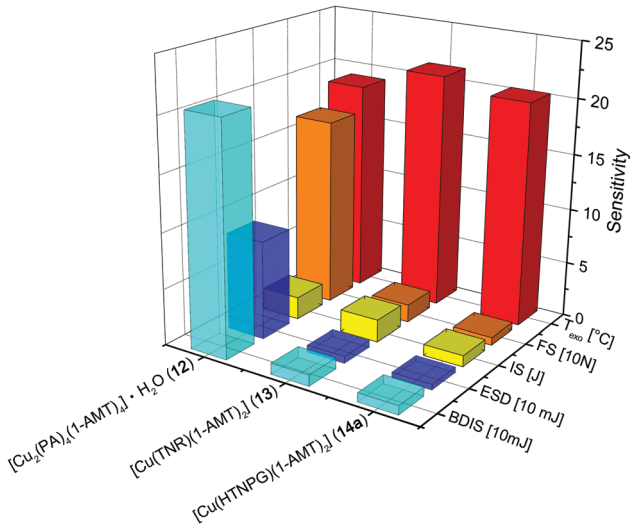

Fig. 14 Comparing the sensitivities against external stimuli of the ECC **12–14a**.

Primary explosive suitability evaluation

In order to get an insight into the compounds' behaviour against fast heating with and without confinement, hot plate (HP) and hot needle (HN) tests were performed with all ECC (Fig. 15 and Fig. S34–S47, ESI‡), except for side species **14b** and **14c**. The results are displayed in Table 1 and furthermore allow a preliminary evaluation of their applicability to be used for the initiation of energetic materials. The most promising compounds in these tests have been found to be the 1-AMT-based copper(II) styphnate (**13**) and 5-hydroxy-2,4,6-trinitroresorcinate (**14a**) complexes, which showed either sharp deflagrations or even detonations in this setup.

For their potential use as lead-free primary explosives, both compounds were tested towards their capability of initiating pentaerythritol tetranitrate (PETN). Therefore, 200 mg of the booster explosive was loaded into a copper shell and the test substance was filled on top (Fig. 16).

More details on the test setup can be found in the General methods of the ESI.‡ Positive transfer of the detonation wave from the primary explosive towards PETN is indicated by a hole in the copper witness plate and fragmentation of the shell. Both compounds were able to initiate nitropenta; whereas **13** worked in our standard setup with pressed PETN, **14a** was only successful in combination with uncompressed PETN (Fig. 16). Due to the known fact that unconfined PETN requires much lower energies than the compressed one,[30] **13** is the more powerful primary explosive compared to **14a**. Additionally, **13** shows a 10 °C higher thermal stability and is slightly less sensitive towards

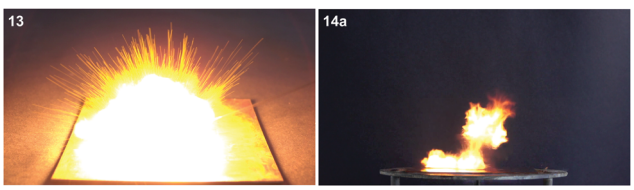

Fig. 15 Moments of deflagration of **13** (left) during hot needle and **14a** (right) during hot plate tests.

Fig. 16 Schematic setup of the PETN initiation capability test (left) as well as positive results of ECC **13** (middle) and **14a** (right).

Table 2 Results of the laser initiation experiments[a]

E_{max} [mJ]	0.17	0.20	0.24	3.00	25.5	30.0	36.0
6	dec.	dec.	—	—	—	—	dec.
7	def.	—	—	—	det.	—	—
8	def.	—	—	def.	—	—	—
9	dec.	dec.	—	—	—	—	dec.
10	def.	def.	—	—	def.	—	—
11	def.	—	—	—	—	def.	det.
12	—	—	—	—	—	dec.	dec.
13	—	—	—	—	dec.	—	dec.
14a	neg.	—	dec.	—	—	dec.	—
15	—	dec.	—	—	—	—	dec.
16	—	—	—	dec.	—	dec.	—
17	dec.	dec.	—	—	—	—	—

[a] Not tested; neg.: no reaction; dec.: decomposition; def.: deflagration; det.: detonation. Operating parameters: voltage U = 4 V; wavelength λ = 915 nm; current I = 7–9 A; pulse length τ = 0.1–15 ms; theoretical maximal output power P_{max} = 45 W; theoretical energy E_{max} = 0.17–36.0 mJ.

all tested external stimuli (IS, FS, ESD, and BDIS) making its manageability safer.

Laser initiation experiments

The most tremendous benefits of laser initiation over classical ignition methods (thermal or mechanical) are the applicability of less sensitive compounds and the resulting lower risk of unintended ignition.[16] Therefore, this research area has gained increasing interest within the energetic material community and a lot of investigations were performed.[17,20,32–34] All complexes, except **14b** and **14c**, were irradiated with an InGaAs laser diode working in single-pulse mode. Details of the applied test setup can be found in the ESI.‡ All examined ECC showed a reaction towards the laser irradiation, differing in the intensity of the outcome (Table 2 and Fig. S48–S59, ESI‡). The most interesting compounds in this investigation are the ones showing both decreased impact and friction sensitivities ($\geq$3 J, $\geq$48 N), which are close to the values of PETN.[29]

These values pose slightly increased sensitivities towards mechanical stimuli but still allow safe handling of the material. Interestingly, all complexes based on AMT ligands solely exhibit decomposition or no reaction at all, regardless of the energy they are irradiated with. In the case of the aminotetrazole compounds, the picrates display the same outcome, whereas the HTNR- and H_2TNPG-based ECC deflagrate at lower energies or can even be detonated (**7** and **11**) when irradiated with higher values. Comparing the more sensitive compounds (**7**, **8**, **11**, **13**, **14a**, and **17**), it becomes clear that the most sensitive ones (**13**, **14a** and **17**) and also the most energetic ones in classical initiation tests (**13** and **14a**) show lower performance in this setup, which is not in accordance with our previous findings.[17,20,22]

UV-vis spectroscopy

UV-vis spectra in the solid state were recorded for the examined ECC **6–17**, except **14b** and **14c**, in the range of 350–1000 nm (Fig. S60–S63, ESI‡), to reveal any possible correlation between the absorption intensity and wavelength of the laser diode. The discovered optical properties of the complexes are summarised in Table 3. All ECC show characteristic transitions in the near infrared, visible and UV regions, as well as moderate to very strong absorption at a laser wavelength of 915 nm. The observed absorptions can mainly be assigned to the d–d transitions of the copper(II) centres. In accordance with previous investigations, the positive reaction towards laser irradiation could be explained by the imaginable formation of several hot spots within the compounds caused by photothermal excitation after irradiation.[16] Interestingly, there is no trend between the absorption intensity at the laser wavelength and the resulting outcome of the irradiation.

Table 3 Summary of the discovered optical properties of the examined ECC **6–17**

Compound	M	Colour	λ_{d-d}[a]	$\lambda_{915}/\lambda_{d-d}$[b]
6	Cu(II)	Green	405	0.45
7	Cu(II)	Green	410	0.65
8	Cu(II)	Green-yellow	356	0.35
9	Cu(II)	Green	424	0.43
10	Cu(II)	Green	412	0.52
11	Cu(II)	Green	437	0.56
12	Cu(II)	Green	431	0.64
13	Cu(II)	Green	459	0.57
14a	Cu(II)	Brown	409	0.53
15	Cu(II)	Green	426	0.68
16	Cu(II)	Green	610	0.97
17	Cu(II)	Green	388	0.40

[a] Absorption intensity maximum wavelength in the observed range of 350–1000 nm, which can be assigned to electron d–d transitions. [b] Quotient of the absorption intensity at the laser wavelength and the intensity at the d–d absorption wavelength.

Conclusions

In this extensive study, the nitrogen-rich ligands 1-amino- (**4a**, 1-AT) and 2-amino-5*H*-tetrazole (**5a**, 2-AT) as well as 1-amino- (**4b**, 1-AMT) and 2-amino-5-methyltetrazole (**5b**, 2-AMT) were successfully applied for the synthesis of new copper(II) complexes. It could be demonstrated that ligands **4b** and **5b** tend to form complexes with higher thermal stability and lower sensitivity. The crystal structures of 16 (12 main products, 2 side species, one ligand, and one precursor) compounds were elucidated by low-temperature single crystal X-ray diffraction and compared in detail. Especially the use of anions based on trinitrophloroglucinol offers a wide range of different complexes with various as well as interesting coordination modes. Furthermore, like styphnic acid, it allows the formation of polymeric structures through the multiple deprotonation of its hydroxy groups, which is accompanied by an increase in thermal stability. Interestingly, the ECC based on the more energetic and more sensitive AT-ligands show better stabilities against external stimuli, such as impact and friction, than the analogous compounds containing AMT derivatives. Whereas complexes **13** and **14a** were able to successfully initiate nitropenta, **7**, **8**, **10**, and **11** show promising results during the laser ignition experiments. Due to their deflagrations at already 0.17 mJ they are interesting candidates for future laser ignition devices, while **13** and **14a** could be potential replacements for lead azide in classic initiation devices. The low performances of the AMT complexes when irradiated with NIR wavelengths

indicate that systems based on copper(II) and nitroaromatic anions with these are not very suitable for laser initiation or need substantially higher energies.

Conflicts of interest

There are no conflicts to declare.

Acknowledgements

Financial support of this work from the Ludwig-Maximilian University of Munich (LMU). The authors would like to thank Prof. Dr Thomas M. Klapötke for his scientific support as well as for providing his research facilities and, furthermore, Prof. Dr Konstantin Karaghiosoff for measuring the ^{15}N NMR spectra. Andreas Bartonek and Jasmin Lechner are given thanks for their great contribution to this work.

Notes and references

1 T. M. Klapötke, *Chemistry of High-Energy Materials*, De Gruyter, Berlin/Boston, 4th edn, 2017.
2 J. Akhavan, *The Chemistry of Explosives*, Royal Society of Chemistry, Cambridge, 2nd edn, 2004.
3 H. Sprengel, *The Discovery of Picric Acid (Melinite, Lyddite) "As a Powerful Explosive" and of Cumulative Detonation with its Bearing on wet Gun Cotton*, Eyre & Spottiswoode, London, 2nd edn, 1903.
4 H. Sprengel, *Br. Pat.*, #901, 1871.
5 J. S. Wallace, *Chemical Analysis of Firearms, Ammunition, and Gunshot Residue*, CRC Press, Boca Raton, 1st edn, 2008.
6 J. P. Agrawal and R. D. Hodgson, *Organic Chemistry of Explosives*, John Wiley & Sons, Hoboken, 1st edn, 2007.
7 M. A. S. Laidlaw, G. Filippelli, H. Mielke, B. Gulson and A. S. Ball, *Environ. Health*, 2017, **16**, 34.
8 R. V. Kent, T. P. Vaid, J. A. Boissonnault and A. J. Matzger, *Dalton Trans.*, 2019, **48**, 7509.
9 Y. Liu, G. Zhao, Y. Tang, J. Zhang, L. Hu, G. H. Imler, D. A. Parrish and J. M. Shreeve, *J. Mater. Chem. A*, 2019, **7**, 7875.
10 E. C. Johnson, E. J. Bukowski, J. J. Sabatini, R. C. Sausa, E. F. C. Byrd, M. A. Garner and D. E. Chavez, *ChemPlusChem*, 2019, **84**, 319.
11 Q. Sun, X. Li, Q. Lin and M. Lu, *J. Mater. Chem. A*, 2019, **7**, 4611.
12 A. A. Larin, N. V. Muravyev, A. N. Pivkina, K. Y. Suponitsky, I. V. Ananyev, D. V. Khakimov, L. L. Fershtat and N. N. Makhova, *Chem. – Eur. J.*, 2019, **25**, 4225.
13 R. Haiges and K. O. Christe, *Dalton Trans.*, 2015, **44**, 10166.
14 J.-G. Xu, X.-Z. Li, H.-F. Wu, F.-K. Zheng, J. Chen and G.-C. Guo, *Cryst. Growth Des.*, 2019, **19**, 3934.
15 J.-G. Xu, C. Sun, M.-J. Zhang, B.-W. Liu, X.-Z. Li, J. Lu, S.-H. Wang, F.-K. Zheng and G.-C. Guo, *Chem. Mater.*, 2017, **29**, 9725.
16 S. R. Ahmad and M. Cartwright, *Laser Ignition of Energetic Materials*, John Wiley & Sons, Ltd., Hoboken, 1st edn, 2015.
17 N. Szimhardt, M. H. H. Wurzenberger, A. Beringer, L. J. Daumann and J. Stierstorfer, *J. Mater. Chem. A*, 2017, **5**, 23753.
18 Y. Cui, T. L. Zhang, J. G. Zhang, L. Yang, J. Zhang and X. Hu, *Propellants, Explos., Pyrotech.*, 2008, **33**, 437.
19 Y. Cui, J. G. Zhang, T. L. Zhang, L. Yang, Y. Zhang and Y. J. Shu, *Chin. J. Chem.*, 2008, **26**, 2029.
20 N. Szimhardt, M. H. H. Wurzenberger, T. M. Klapötke, J. T. Lechner, H. Reichherzer, C. C. Unger and J. Stierstorfer, *J. Mater. Chem. A*, 2018, **6**, 6565.
21 Y. G. Bi, Y. A. Feng, Y. Li, B. D. Wu and T. L. Zhang, *J. Coord. Chem.*, 2015, **68**, 181.
22 M. H. H. Wurzenberger, M. S. Gruhne, M. Lommel, N. Szimhardt, T. M. Klapötke and J. Stierstorfer, *Chem. – Asian J.*, 2019, **14**, 2018.
23 Y. Cui, J. G. Zhang, T. L. Zhang, L. Yang, J. Zhang and X. Hu, *J. Hazard. Mater.*, 2008, **160**, 45.
24 N. Szimhardt, M. H. H. Wurzenberger, L. Zeisel, M. S. Gruhne, M. Lommel, T. M. Klapötke and J. Stierstorfer, *Chem. – Eur. J.*, 2019, **25**, 1963.
25 N. Szimhardt, M. H. H. Wurzenberger, L. Zeisel, M. S. Gruhne, M. Lommel and J. Stierstorfer, *J. Mater. Chem. A*, 2018, **6**, 16257.
26 Crystallographic data for the structures has been deposited with the Cambridge Crystallographic Data Centre. Copies of the data can be obtained free of charge on application to The Director, CCDC, 12 Union Road, Cambridge CB2 1EZ, UK (Fax: int.code_(1223)336-033; e-mail for inquiry: fileserv@ccdc.cam.ac.uk; e-mail for deposition: (deposit@ccdc.cam.ac.uk)).
27 M. Daszkiewicz, *CrystEngComm*, 2013, **15**, 10427.
28 T. M. Klapötke, D. G. Piercey and J. Stierstorfer, *Dalton Trans.*, 2012, **41**, 9451.
29 T. M. Klapötke, *Energetic Materials Encyclopedia*, 1st edn, De Gryter, Berlin/Boston, 2018.
30 R. Matyáš and J. Pachman, *Primary Explosives*, Springer, Berlin, 1st edn, 2013.
31 Impact: insensitive $>$ 40 J, less sensitive $\geq$ 35 J, sensitive $\geq$ 4 J, very sensitive $\leq$ 3 J; friction: insensitive $>$ 360 N, less sensitive = 360 N, sensitive $<$ 360 N and $>$ 80 N, very sensitive $\leq$ 80 N, extremely sensitive $\leq$ 10 N. According to the UN Recommendations on the Transport of Dangerous Goods.
32 D. E. Chavez, S. K. Hanson, R. J. Scharff, J. M. Veauthier and T. W. Myers, *US Pat.*, 20160031767A1, Triad National Security LLC, 2015.
33 S. I. Gerasimov, M. A. Ilyushin, I. V. Shugalei, A. V. Smirnov and Z. V. Kapitonenko, *Russ. J. Gen. Chem.*, 2017, **87**, 3156.
34 W. Guo, L. Wu, N. He, S. Chen, W. Zhang, R. Shen and Y. Ye, *Laser Part. Beams*, 2018, **36**, 29.

